Surface structure and electronic states of epitaxial β-$FeSi_2$(100)/Si(001) thin films: Combined quantitative LEED, *ab initio* DFT, and STM study

O. Romanyuk*
Institute of Physics, Academy of Sciences of the Czech Republic, Cukrovarnická 10, 16200 Prague, Czech Republic

K. Hattori, M. Someta, and H. Daimon
Graduate School of Materials Science, Nara Institute of Science and Technology, Takayama 8916-5, Ikoma, Nara 630-0192, Japan
(Received 28 April 2014; revised manuscript received 18 July 2014; published 13 October 2014)

The surface structure of epitaxial β-$FeSi_2$(100) thin film grown on Si(001) was analyzed using the quantitative low-energy electron diffraction intensity-voltage (LEED I-V) method, *ab initio* density functional theory (DFT) calculations, and scanning tunneling microscopy (STM). LEED patterns measured on the β-$FeSi_2$(100) surface reveal two domains of a $p(2 \times 2)$ reconstruction with $p2gg$ diffraction symmetry. The iron-silicide film truncation and atomic surface structure were determined by LEED I-V method: The smallest Pendry's reliability factor $R_P = 0.22 \pm 0.02$ was achieved for the bare β-$FeSi_2$ film truncated by an Si layer, whereas Si and Fe ad-atom structures were excluded. Significant atomic relaxations within the topmost surface layers were revealed by the LEED I-V method and confirmed by DFT. The simulated STM patterns from the best-fit model agree well with the measured STM images on the β-$FeSi_2$(100)/Si(001)-$p(2 \times 2)$ surface: Four Si atoms on a surface form one bright protrusion on STM patterns. Electronic band structure analysis of the bulk and epitaxial β-$FeSi_2$(100) was carried out. A bare truncated epitaxial film was found to be metallic. Surface electronic states were identified by a partial k-resolved atomic-orbital based local density-of-state analysis.

DOI: 10.1103/PhysRevB.90.155305 PACS number(s): 68.35.B−, 81.15.Np, 68.37.Ef, 68.55.−a

I. INTRODUCTION

Iron silicides grown on silicon substrates have attracted great interest due to applications in opto- and microelectronics [1,2]. Iron silicides cover a wide range of electronic properties because they can exist in semiconducting, metallic, and ferromagnetic phases depending on epitaxial film thickness and preparation conditions, e.g., amount of deposited Fe on the Si substrate and subsequent annealing procedures [3–7]. Despite recent progress in the understanding of iron-silicide fabrication conditions, there is only limited knowledge about the atomic structure of the iron-silicide surfaces.

The iron-silicide thin films can be prepared using a variety of methods such as solid-phase epitaxy (SPE) [8–13], co-deposition by molecular-beam epitaxy [14], reactivity deposition epitaxy [15,16], and high-temperature flash annealing [17]. The iron-silicide film quality and its surface morphology strongly depend on preparation conditions. Good quality of the film can be achieved with the SPE method. Schematic phase diagrams of iron-silicide films grown by SPE on Si(001) [10–12] and Si(111) [13] substrates consist of several different phases with two-dimensional or three-dimensional islands on the surfaces.

The two-dimensional semiconducting β-$FeSi_2$ phase has been studied intensively in the past [18]. The bulk phase shows an indirect band gap of 0.85 eV. On the other hand, strained phases such as two-dimensional β-$FeSi_2$(100) film grown on Si(001) have a direct band gap [19] and, therefore, the β-$FeSi_2$ phase is suitable for the production of optoelectronic devices [1].

Formation of the β-$FeSi_2$(100) films on Si(001) surfaces was investigated by electron diffraction [20–23] and x-ray diffraction (XRD) [23,24] methods. Two possible types of heteroepitaxial relationships of β-$FeSi_2$ films on the Si(001) substrate were confirmed: type-A film orientation is β-$FeSi_2$[010] ∥ Si⟨110⟩ and type-B orientation is β-$FeSi_2$[010] ∥ Si⟨100⟩ [21]. Since type A is more stable than type B, the majority of studies are related to the type-A films. It was reported that the β-$FeSi_2$[010] ∥ Si⟨110⟩ surface is terminated by $c(2 \times 2)$-like [21] or $p(2 \times 2)$ reconstructions [21,24].

SPE-grown two-dimensional iron-silicide islands on Si(001) were observed with scanning tunneling microscopy (STM) [11,25,26]. Iron-silicide islands terminated by $c(2 \times 2)$-like protrusions were surrounded by Si(001)-(2×1) dimers. Two-dimensional islands were identified as the β-$FeSi_2$(100) phase [25]. The thin film iron-silicide phase diagram, however, involves many phases, which could coexist with double-domain Si(001)-(2×1) reconstruction of the substrate. Phase coexistence complicates the surface structure analysis. Therefore, preparation of a single phase thin iron-silicide film is crucial for macroscopic analysis by low-energy electron diffraction (LEED), reflection high-energy electron diffraction (RHEED), XRD, or low-energy ion scattering (LEIS) spectroscopy [11].

The atomic structure of the bulk β-$FeSi_2$ is well known, whereas surface structures of the epitaxial β-$FeSi_2$ films or single crystalline β-$FeSi_2$ are still less understood. The surface structure of single-crystalline β-$FeSi_2$(100) was studied using LEED, STM and *ab initio* calculations based on density functional theory (DFT) [27,28]. STM images and LEED patterns measured on single-crystal surfaces [27] were found to be almost the same as those measured on the SPE-grown iron-silicide island surfaces: the $c(2 \times 2)$-like surface protrusions

*romanyuk@fzu.cz

were confirmed in both cases by STM. Since the β-$FeSi_2(100)$ surface unit cell is two times larger than the Si(100)-(1×1) surface unit cell in a real space and is not rotated with respect to the Si surface unit cell, such a surface has actually a $p(2 \times 2)$ periodicity [21].

Bare truncated iron-silicide surfaces were studied with *ab initio* DFT calculations [28]. Five possible bulk-like truncated surface models (without adatoms) were considered. It was found that surface atoms relax to a square-like unit reproducing experimental STM patterns. However, detailed atomic positions were not given. To discuss the reliable surface structure models, it is useful to extend theoretical studies using experimental approaches and to derive atomic positions on a surface. So far, the Si termination of the epitaxial β-$FeSi_2(100)$ film was confirmed experimentally by LEIS [24]. Details of surface reconstruction were not derived, however.

In the present paper, two-dimensional thin β-$FeSi_2(100)$ film with high coverage on Si(001) substrate was prepared and investigated with the quantitative LEED intensity-voltage (LEED I-V) method, STM, and *ab initio* DFT calculations. Surface models with adatoms on a surface and bare iron-silicide structure models were considered. Good agreement between the experimental and theoretical LEED I-V curves was achieved for one surface structure model only. Measured STM images of iron-silicide surfaces were interpreted based on the simulated STM patterns from the relaxed best-fit structure model. Electronic band structure including surface states due to film truncation of the relaxed best-fit model was derived.

II. EXPERIMENTAL PART

The β-$FeSi_2(100)$/Si(001) film was prepared using the SPE method in an ultrahigh vacuum (UHV) system equipped with LEED optics (OCI, BDL600IR) and STM (UNISOKU, USM612SA2, and RHK, SPM1000) [11–13]. An Si(001) wafer (Sb doped, 0.03 Ω cm) was degassed and flashed at 1250 °C a few tens times with direct-current heating until clear Si(001)-$(2 \times 1)/(1 \times 2)$ double-domain LEED patterns appeared. The pressure in the chamber during the flashing was below $2–3 \times 10^{-8}$ Pa. Four monolayers (ML) of Fe (99.999%) were deposited onto the clean Si(001)-$(2 \times 1)/(1 \times 2)$ surface at room temperature using an alumina-crucible evaporator. The unity ML of Fe corresponds to 6.78×10^{14} atoms/cm^2. The deposition rate was approximately 0.3 ML per minute. The pressure in the chamber was less than 5×10^{-8} Pa during the deposition. The sample was annealed at 450 °C for 10 minutes, monitored by a pyrometer. After the annealing, the sample temperature was decreased to room temperature (RT). A $p(2 \times 2)$ diffraction pattern was observed by LEED on the surface.

LEED patterns were measured at RT with a 16-bit CCD camera and stored in the memory of the computer together with the value of the primary beam current. Diffraction patterns were recorded with a 1 eV step in the energy range of 30–300 eV. LEED I-V curves of 14 non-equivalent beams were measured from the LEED patterns. The diffraction intensities of each spot were normalized on a primary electron beam current. Background intensity around each diffraction spot was subtracted.

Topographic STM measurements were carried out at RT by using a chemically etched W tip. Details of the STM measurements can be found elsewhere [12].

III. COMPUTATIONAL DETAILS

Dynamical LEED I-V curve calculations were carried out using the SATLEED package [29]. Scattering on single atoms was calculated by relativistic phase shifts [30] with the highest angular momentum quantum number $l_{max} = 7$. Electron wave damping inside the crystal due to inelastic electron scattering was represented in the calculations by the imaginary part of the inner potential equal to −4.0 eV. The real part of the inner potential of −8.7 eV was adjusted during the structure analysis. Finite temperature contributions to diffraction intensities were included in the calculation through the isotropic atomic vibrations, namely by means of the Debye-Waller factor. The vibration amplitudes u(Fe) and u(Si) were assumed to be equal to 0.065 Å and 0.077 Å, respectively. Atomic coordinates of the models were adjusted until a smallest Pendry's reliability factor [31], R_P, was obtained. The statistical error bars were estimated for the total LEED I-V curves energy range of 2513 eV.

The ideal β-$FeSi_2(100)$ surface has a $p2gg$ [32] symmetry. The $p2gg$ symmetry and two domains on a surface were confirmed by the LEED experiments (as described later). Thus in the LEED I-V calculations, the surface structure models with $p2gg$ symmetry were analyzed. Symmetrically equivalent theoretical LEED I-V curves were averaged for two domains. Atomic slab of the β-$FeSi_2(100)$ consisting of 11 layers was used. A perturbation scheme based on the trial-and-error search algorithm [33] was used in order to reduce the R_P. Since glide plane symmetry operations are not involved in the search algorithm in the SATLEED program [29], structure refinement was carried out in two steps [34,35]. First, a full dynamical LEED I-V calculation was carried out for the initial structure model with $p2gg$ symmetry (step 1). Second, atomic positions were adjusted with a $p2$ symmetry restriction only. After the R_P-factor minimum was achieved, the $p2gg$ symmetry of the relaxed structure was recovered by averaging the corresponding atomic position deviations (step 2). Full dynamical LEED I-V calculation (step 1) and position adjustment with the symmetry recovering procedure (step 2) were repeated until the convergence of R_P was achieved after the first calculation step only, i.e., the final structure has $p2gg$ symmetry.

STM images of the best-fit surface model were simulated with the Simulation Tool for Atom TEchnology (STATE)-Senri program [36]. *Ab initio* DFT calculations within the generalized gradient approximation [37] were performed. The structure was relaxed by using the Troullier-Martins norm-conserving pseudopotentials for Si and Fe atoms. The wave functions and charge densities were expanded by a plane-wave set with cutoff energies of 25 and 225 Ry, respectively. A $5 \times 5 \times 1$ $(5 \times 5 \times 5)$ k-point mesh was used for the k-space integration within a surface slab (bulk). The iron-silicide slab consisted of 12 layers (11.5 Å) and a vacuum gap region of 20.3 Å. Atomic positions were relaxed until all residual force components were less than 0.05 eV/Å. The bottom of the slab was terminated by H atoms. The three bottom layers of the slab (Fe-Si-H) were fixed. The spin polarization was not taken into account in the calculations.

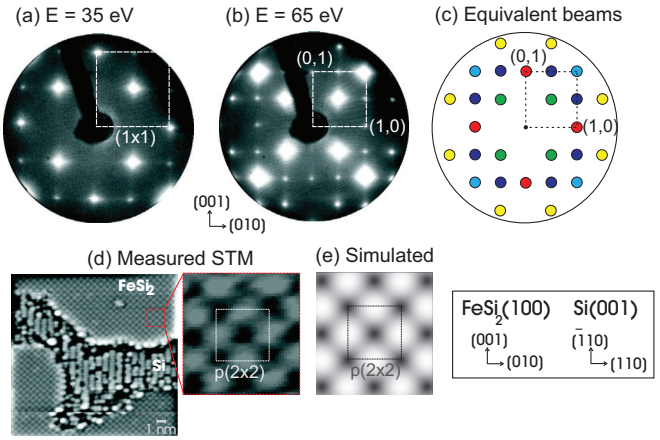

FIG. 1. (Color online) LEED patterns measured on the epitaxial β-$FeSi_2(100)$/Si(001)-$p(2\times2)$ surface at electron beam energies of (a) $E = 35$ eV and (b) $E = 65$ eV. A Si(001)-(1×1) unit cell is marked with a dashed square. $(h/2,0)$ and $(0,k/2)$ reflections, where h and k are odd integers, are forbidden due to $p2gg$ symmetry. Equivalent diffraction beam intensities are shown schematically using circles of the same color in (c). Two 90°-rotated equivalent domains of iron silicide were confirmed on a surface. (d) Measured and (e) simulated filled state ($U = -1.5$ V) STM images of the β-$FeSi_2$ surface. Si(001) substrate with (2×1) protrusions is seen in (d). A magnified region of the β-$FeSi_2$ film is shown; a $p(2\times2)$ unit cell of 7.8 Å × 7.8 Å area is marked by a white square. Each bright protrusion is formed by four Si atoms on a surface [see relaxed layer 1 in Fig. 2(b)]

IV. RESULTS AND DISCUSSION

A. Atomic structure analysis

LEED patterns measured with primary electron beam energies of $E = 35$ eV and $E = 65$ eV on the β-$FeSi_2(100)$/Si(001)-$p(2\times2)$ surface are shown in Figs. 1(a) and 1(b), respectively. There are sharp diffraction peak maxima and low background intensity on the LEED patterns. A Si(001)-(1×1) surface unit cell is marked by a dashed square in Figs. 1(a) and 1(b). The β-$FeSi_2(100)$ surface unit cell forms a $p(2\times2)$ unit with respect to the Si(001)-(1×1) surface unit cell because the iron-silicide lattice constant is close to two silicon lattice constants, $2a_{Si} = 7.68$ Å (see Fig. 2).

Reflections $(h/2,0)$ and $(0,k/2)$, where h and k are odd integers, were absent on all LEED patterns in the measured energy range (Fig. 1). These forbidden reflections exclude the $p2$ symmetry and confirm the $p2gg$ symmetry on a surface [38]. Similar LEED pattern symmetry was observed on a single crystalline β-$FeSi_2$ surface [27] (note, without Si substrate): Patterns confirmed a (1×1) periodicity in respect to the single crystalline β-$FeSi_2$ substrate. In the present work, diffraction spot notation with respect to the Si substrate was used.

Intensities of the $(h/2,k/2)$, $(h/2,-k/2)$, $(k/2,h/2)$ and $(k/2,-h/2)$ reflections were found to be equivalent on experimental LEED patterns. A schematic view of observed symmetrically equivalent LEED intensities (classified by colors) is shown in Fig. 1(c). Note, the experimental $(1,1/2)$ and $(1/2,1)$ spot intensities were equivalent, for instance. It could not be achieved by applying the $p2$ symmetry operations only (without mirror or glide plane symmetry) even for structures with two 90°-rotated domains. Since mirror plane symmetry operations are absent for the β-$FeSi_2(100)$ lattice, only the presence of glide plane symmetry operation (Fig. 2) and two domains on a surface can explains the observed equivalent intensities. Two domains on iron-silicide surface were caused by a double-domain structure on a Si(001) substrate, i.e., atomic monolayer steps on Si(001) substrate. The first single domain with $p2gg$ symmetry leads to four equivalent reflections $(1,1/2)$, $(1,-1/2)$, $(-1,1/2)$, and $(-1,-1/2)$. The second rotated domain leads to equivalent reflections $(1/2,1)$, $(1/2,-1)$, $(-1/2,1)$, and $(-1/2,-1)$. In case of two equivalent domains on a surface, the $(1,1/2)$ and $(1/2,1)$ reflections have to be equivalent. Thus, the $p2gg$ symmetry and two domains rotated 90° to each other were confirmed on the β-$FeSi_2(100)$ surface by LEED.

There are cross-like diffuse streaks around the diffraction spot maxima along the β-$FeSi_2$ [001] and [010] directions on the LEED patterns [Figs. 1(a) and 1(b)]. Diffuse intensities are suppressed on LEED patterns measured on a single-crystal surface [39]. Such diffuse streaks could be a strain induced effect [40] due to β-$FeSi_2(100)$ film relaxation on the Si(001) substrate. There is a 2% (1.5%) misfit between the β-$FeSi_2(100)$ and Si(001) lattice constants along the β-$FeSi_2$[001] ([010]) direction. In-plane interatomic distance relaxations are expected for thin iron-silicide films. In LEED I-V analysis, diffraction spot intensities in proximity of the spot maxima were used. In this region, diffuse streak intensity contributions are negligible in comparison with diffraction peak intensity maxima and do not influence the analysis.

Experimental LEED I-V curves were derived using diffraction spot intensity integration around the diffraction peak maxima on LEED patterns. Diffraction intensities of symmetrically equivalent beams were averaged [Fig. 1(c)]. Fourteen nonequivalent experimental LEED I-V curves are shown by black curves in Fig. 3.

In Fig. 1(d), the filled state STM image (sample-bias voltage $U = -1.5$ V) measured on the β-$FeSi_2(100)$/Si(001) thin-film surface is presented. Similar STM patterns were observed on iron-silicide films in the past [11,25,26]. A $p(2\times2)$ surface unit cell consists of two bright protrusions per surface unit cell (marked with a square), and, therefore, such STM patterns were called $c(2\times2)$-like patterns. Nevertheless, the pattern has $p(2\times2)$ periodicity with respect to the Si(001) substrate.

β-$FeSi_2$ film coverage of 88% and an average domain size of approximately 200 Å were evaluated from the STM measurements. The Si substrate was covered by almost a single phase of β-$FeSi_2$. In Fig. 1(d), a quite rare part of uncovered Si substrate with Si dimers close to the iron-silicide edge is shown. The uncovered part of the Si(001) substrate was found to be purely ordered by Si dimers. Otherwise, the surface is mainly covered by well-ordered iron-silicide film.

The atomic structure of the bulk orthorhombic β-$FeSi_2$ unit cell is shown in Fig. 2. In-plane unit cell translation vectors $|\mathbf{b}| = 7.79$ Å, $|\mathbf{c}| = 7.83$ Å and the out-of-plane translation vector $|\mathbf{a}| = 9.86$ Å are indicated. The [010] and [001] azimuthal directions of the β-$FeSi_2(100)$ are aligned along the [110] and $[\bar{1}10]$ directions of the Si(001) substrate, respectively [25]. The β-$FeSi_2$ bulk unit cell consists of ten subplanes with 48 atoms in total [Fig. 2(a)].

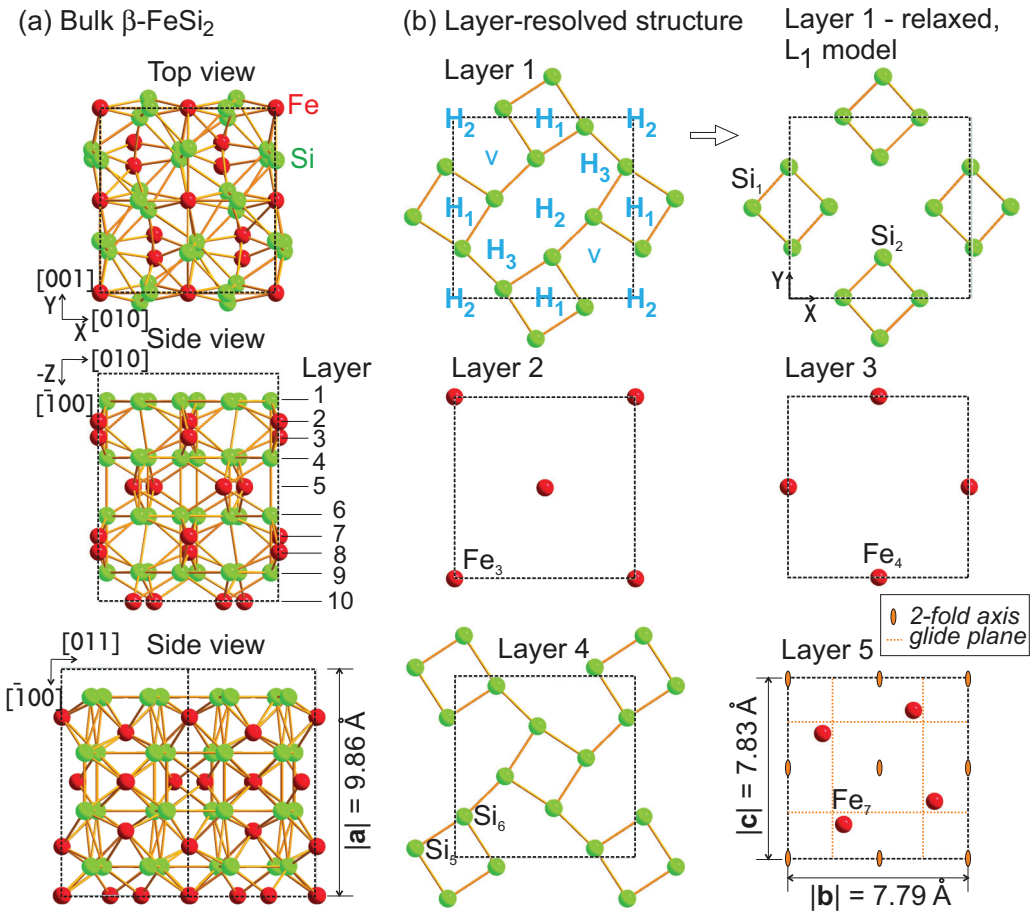

FIG. 2. (Color online) (a) Top and side views of bulk β-$FeSi_2$ unit cells. Fe and Si atoms are marked with red and green spheres, respectively. Layers 6–10 are shifted with respect to layers 1–5 by $|\mathbf{b}|/2$ distance along the [010] direction. Layer-resolved structures of bulk unit cells are shown in (b). The adatom models consist of Si or Fe atoms on H_1, H_2 sites. The $p2gg$ symmetry is preserved for bare truncated and adatom H_1, H_2 structure models. The H_3 model with vacancies (v) has $p2$ symmetry. Twofold rotation axis and glide planes are indicated (layer 5). The glide operations translate atoms along the glide planes by $|\mathbf{b}|/2$ or $|\mathbf{c}|/2$, and mirror them against these planes. The topmost relaxed layer of the best-fit L_1 model is shown on the right-hand side of layer 1. The coordinates of the relaxed structure are presented in Table II.

The layer-resolved structures of a bulk unit cell are shown in Fig. 2(b). The first layer consists of eight Si atoms within the in-plane unit cell. The structure obeys $p2gg$ symmetry, which includes glide plane translation operations and a twofold rotation axis (marked on layer 5). The $p2gg$ symmetry was also confirmed by the LEED measurements [Fig. 1(a)], as mentioned. The second and the third layers consist of two Fe atoms per in-plane unit cell. The fourth Si layer is the same as the first Si layer, but it is shifted on the $|\mathbf{b}|/2$ vector along the [010] direction. The fifth layer consists of four Fe atoms. The atomic structures of the planes 6–10 are the same as the atomic structures of the planes 1–5, but the planes are shifted on vector $|\mathbf{b}|/2$ along the [010] direction. Thus, the bulk β-$FeSi_2$ unit cell consists of two groups of planes, which are shifted relative to each other.

Bare (bulk-like) truncated and adatom iron-silicide surface structure models were considered for LEED I-V analysis. A bare iron-silicide film can be truncated by layers 1, 2, 3, 4, and 5 [Fig. 2(b)]. Surface truncation by Fe layers (2, 3, or 5) was excluded by LEIS measurements [24]. Nevertheless, all possible nonequivalent β-$FeSi_2$ bulk-like truncations by layers 1 (L_1), 2 (L_2), 3 (L_3), 4 (L_4), and 5 (L_5) were considered in the present paper.

The adatom models consist of two Si or Fe adatoms per surface unit cell on top of the bare surface, leading to the $c(2 \times 2)$-like arrangement. Adatoms can be situated on H_1, H_2, and H_3 hollow sites [Fig. 2(b)] on top of L_1, L_2, L_3, L_4, and L_5 layers. The $p2gg$ symmetry must be preserved for all surface structure models according to LEED measurements.

A structure with adatoms on the H_3 site and $p2gg$ symmetry consists of four (not two) adatoms per surface unit cell, since the glide plane symmetry operations put adatoms on two additional vacancy sites (v). Such a structure has (1×1) periodicity with respect to the Si substrate. On the other hand, the H_3 model with two vacancies and two adatoms on H_3 sites ($p2$ symmetry) [Fig. 2(b)] could correspond to the $c(2 \times 2)$-like protrusions observed by STM. In this case, however, LEED spot extinction due to $p2gg$ symmetry is not expected. Thus, the H_3 site adatom structure models were excluded. Therefore, 20 adatom and 5 bare surface structure models were considered in total.

We found that the best-fit structure is terminated by the Si layer (L_1) without adatoms. This structure produces the smallest R_P factor of 0.22 ± 0.02 (Table I). The best-fit theoretical LEED I-V curves for 14 non-equivalent reflections

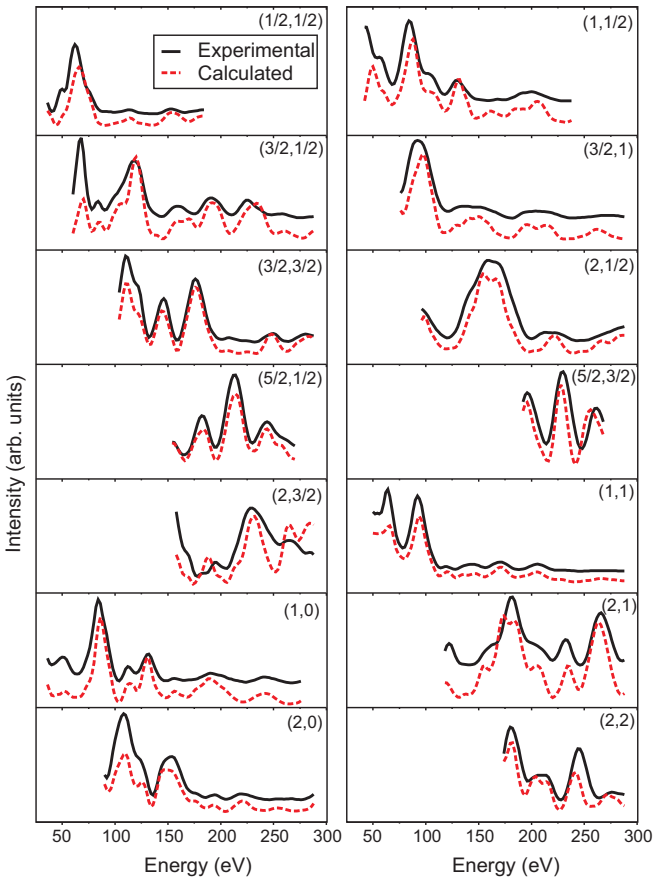

FIG. 3. (Color online) Comparison of experimental (black) and theoretical (red dashed) LEED I-V curves of the best-fit Si-bare model of the β-$FeSi_2(100)/Si(001)$-$p(2\times2)$ surface. Pendry's reliability factor $R_P = 0.22 \pm 0.02$ was achieved for the Si-bare structure with $p2gg$ symmetry. Symmetrically equivalent reflections were averaged according to a scheme presented in Fig. 1(c).

(including two equivalent domains of β-$FeSi_2$) are presented by red dashed curves in Fig. 3. Adatom structure models consisting of Si or Fe adatoms on L_1-L_5 layers and other bare-terminated structure models (L_2-L_5) produced much higher R_P and were excluded.

TABLE I. Pendry's reliability factors, R_P, for the bare (bulk-like) truncated and adatom models of the β-$FeSi_2(100)/Si(001)$-$p(2\times2)$ surface. The bare terminated models include the structures terminated by layers 1 (L_1), 2 (L_2), 3 (L_3), 4 (L_4), and 5 (L_5) [Fig. 2(b)]. The adatom models consist of Fe or Si adatoms on positions H_1, H_2 on top of L_1. Structures with adatoms on layers L_2–L_5 were computed, but not included in the table ($R_P > 0.40$). All adatom models have high R_P and can be excluded. The L_1 model is the most favorable structure.

Bare models		Adatom models	
Structure	R_P	Structure	R_P
L_1	0.22 ± 0.02	L_1-Fe-H_1	0.55 ± 0.06
L_2	0.55 ± 0.06	L_1-Fe-H_2	0.58 ± 0.07
L_3	0.57 ± 0.06	L_1-Si-H_1	0.53 ± 0.06
L_4	0.67 ± 0.08	L_1-Si-H_2	0.60 ± 0.07
L_5	0.68 ± 0.08		

The relaxed topmost layer of the L_1 model is shown in Fig. 2(b). Groups of four Si atoms are rotated with respect to their bulk positions. Si atoms relax in a more symmetrical configuration on the surface. Such relaxation of the topmost Si atoms agrees qualitatively with the structure model recently suggested by *ab initio* DFT calculations [28]. In addition, surface termination by the Si layer agrees with the LEIS measurements [24].

The atomic positions of the relaxed L_1 structure model and their deviations from bulk positions obtained by LEED I-V analysis are included in Table II. Significant atomic relaxations occur within the first three layers on a surface. Small atomic relaxations (less than 0.12 Å) were obtained for the deeper layers.

The L_1 structure model was analyzed by using *ab initio* DFT calculations. Atomic positions of the bulk-like truncated L_1 structure were relaxed. In Table II, atomic deviations from the corresponding bulk positions of the relaxed L_1 model are given in parentheses. The relaxed atomic positions agree well with the corresponding positions, which were derived by the LEED I-V method. There is a small difference in atomic relaxation for the Fe_4 atom only. Other atoms show similar relaxations within error bars of the LEED I-V method. Thus, the relaxed L_1 structure was also confirmed by *ab initio* DFT calculations.

In Fig. 1(e), a simulated filled-state STM pattern from the relaxed L_1 structure model is shown. A $p(2\times2)$ surface unit cell is marked with a square on the pattern. There are two bright protrusions per $p(2\times2)$ surface unit cell. Four Si atoms of a topmost layer produce one bright protrusion on the STM patterns. The simulated STM patterns ($U = -1.5$ V) agree well with the measured STM images [Fig. 1(d)] and with STM images in the literature [11,25,26]. Thus, the relaxed L_1 surface structure model reproduces the experimentally observed STM patterns.

Finally, β-$FeSi_2(100)$ film truncation and atomic surface structure were analyzed by the LEED I-V method, *ab initio* DFT calculations, and STM. We found that the epitaxial β-$FeSi_2(100)$ film is truncated by the L_1 layer, whereas L_2–L_5 layer truncations or adatom structure models were found to be unfavorable. The $p2gg$ symmetry is preserved on the β-$FeSi_2(100)$ surface. Atomic positions on a surface were derived from experimental data and confirmed by theoretical approaches.

B. Electronic band structure analysis

The electronic properties of the semiconductor epitaxial film can be influenced by its atomic surface structure [41]. In particular, the surface induced electronic states in the band gap region can induce surface conductivity of the semiconducting film. Since β-$FeSi_2$ bulk is a narrow band gap semiconductor, surface state formation in proximity of the band gap can change electronic properties crucially. In the following section, surface states due to film truncation are analyzed.

The bulk β-$FeSi_2$ lattice belongs to the $Cmce$ crystallographic space group (number 64) and the $mmmC$ (**a** > **b**) crystal class. Its bulk Brillouin zone (BBZ) is shown in

TABLE II. Atomic positions and their deviations from bulk positions of the best-fit L_1 structure model. Only symmetrically nonequivalent positions are given. The equivalent positions are (X,Y), $(-X,-Y)$, $(X+|\mathbf{b}|/2,-Y+|\mathbf{c}|/2)$, and $(-X+|\mathbf{b}|/2,Y+|\mathbf{c}|/2)$. Atomic position deviations derived by *ab initio* DFT calculations are given in parentheses. Good agreement between LEED I-V and DFT relaxed atomic positions is obtained for the L_1 structure model.

	Fitted atomic positions (Å)			Deviations from bulk (Å)		
Atom	X	Y	Z	ΔX	ΔY	ΔZ
Si_1	-1.64 ± 0.10	3.88 ± 0.06	-0.01 ± 0.02	0.12 (0.06)	0.36 (0.39)	0.00 (0.00)
Si_2	3.97 ± 0.07	1.74 ± 0.11	-0.02 ± 0.03	−0.28 (–0.36)	−0.03 (–0.06)	−0.02 (0.00)
Fe_3	0.00	0.00	-0.88 ± 0.02			−0.02 (–0.01)
Fe_4	3.89	0.00	-1.91 ± 0.05			−0.35 (–0.25)
Si_5	-1.68 ± 0.15	0.39 ± 0.15	-2.48 ± 0.05	0.08 (0.01)	−0.01 (–0.02)	−0.07 (–0.06)
Si_6	0.43 ± 0.12	1.80 ± 0.11	-2.50 ± 0.03	0.08 (0.02)	0.03 (–0.01)	−0.08 (–0.03)
Fe_7	2.30 ± 0.12	1.43 ± 0.13	-3.77 ± 0.04	−0.10 (0.01)	−0.02 (0.02)	−0.09 (–0.07)
Si_8	0.35 ± 0.15	1.77 ± 0.16	-4.97 ± 0.05	0.00 (0.01)	0.00 (0.00)	−0.04 (–0.04)
Si_9	-1.84 ± 0.15	0.41 ± 0.16	-4.98 ± 0.05	−0.08 (0.00)	0.01 (–0.01)	−0.04 (–0.06)
Fe_{10}	3.89	0.00	-5.84 ± 0.06			−0.05 (–0.07)
Fe_{11}	7.79	0.00	-6.55 ± 0.04			−0.06 (–0.07)
Si_{12}	2.26 ± 0.26	0.34 ± 0.21	-7.33 ± 0.15	0.12 (0.00)	−0.06 (–0.02)	0.01 (–0.04)
Si_{13}	4.32 ± 0.25	1.79 ± 0.30	-7.36 ± 0.14	0.07 (0.00)	0.02 (0.01)	−0.01 (–0.05)

Fig. 4(a). The unit cell translation vectors $|\mathbf{a}^*| = 0.64$ Å^{-1}, $|\mathbf{b}^*| = 0.81$ Å^{-1}, and $|\mathbf{c}^*| = 0.80$ Å^{-1} lie along the Γ-Y, Γ-Δ_0, and Γ-Z directions, respectively. The Y, Z, S, and Δ_0 points correspond to $\mathbf{a}^*$, $\mathbf{c}^*/2$, $(\mathbf{a}^*+\mathbf{b}^*)/2$, and $0.81\mathbf{b}^*$.

The growth direction of the epitaxial β-$FeSi_2$ film on Si(001) is the [100] direction (along the $\mathbf{a}^*$ direction) Thus, vector $\mathbf{a}^*$ appoints a surface normal and therefore it is perpendicular to the surface Brillouin zone (SBZ). The irreducible SBZ is marked with a blue rectangle in Fig. 4(a) (shifted for clarity). The surface unit cell vectors in the reciprocal space are $\mathbf{c}^*/2$ and $\mathbf{b}^*/2$ along the $\overline{\Gamma}$-$\overline{X}$ and $\overline{\Gamma}$-$\overline{X}'$ directions, respectively. Note that the SBZ area is smaller than the projected BBZ area along the [010] direction. The BBZ bands, which are situated outside the SBZ, were folded and projected onto the SBZ cell [42].

In Fig. 4(b), the computed bulk band structure of the β-$FeSi_2$ crystal is shown. The zero energy level (dashed line) is referred to the Y point valence band maximum. The computed electronic band structure agrees well with the band structure in the literature [43]. The indirect nature of the fundamental band gap Y-0.6Λ was confirmed for the β-$FeSi_2$ bulk crystal. A computed band gap value of 0.741 eV agrees well with a value of 0.731 eV in Ref. [43].

In Fig. 4(c), the surface band structure of the L_1 model is shown along the $\overline{X}'$-$\overline{\Gamma}$-$\overline{X}$ and $\overline{\Gamma}$-$\overline{M}$ directions. The grey shaded areas represent the bulk projected states. The band gap of 0.741 eV between the shaded bulk valence and conduction bands is seen. The electronic states of the L_1 structure model are represented by black dots. In contrast to the bulk projected bands, a few states appeared in the band gap region (positive energies) and some of them cross the Fermi level (dashed line). Thus, the metallic nature of the β-$FeSi_2$ epitaxial film is predicted. The identification of surface states inside the valence and conduction bands is, however, not straightforward due to the large number of electronic states. Therefore, we suggest the k-resolved atomic-orbital based local density-of-states (k-AO-LDOS) analysis [44] for the identification of surface states.

A k-AO-LDOS, $\rho(k,E,i,l)$, is a function of a wave vector k, energy E, atom species i, and orbital of the ith atom l. k-AO-LDOS was computed within 1.17 Å muffin-tin radii of the atom and was averaged over the LDOS of atoms (the number of which is N) within a layer (or a slab) and summed over the corresponding orbitals of the atoms. A k-AO-LDOS per group of atoms is defined as

$$\rho(k,E) = \frac{1}{N}\Sigma_i \Sigma_l \rho(k,E,i,l). \quad (1)$$

The atomic orbitals l run over the s, p, and d orbital components. i runs over all atoms in a slab, $\rho_{\mathrm{tot}}(k,E)$, $N_{\mathrm{tot}} = 64$, for the total number of atoms; or the topmost atoms only, $\rho_{\mathrm{surf}}(k,E)$, $N_{\mathrm{surf}} = 8$, for the surface. In order to enhance the k-AO-LDOS weight of the particular layer, i.e., surface state components on the plot, the surface k-AO-LDOS was squared and normalized on the total k-AO-LDOS. Partial k-AO-LDOS was defined as

$$\rho'(k,E) = \frac{N_{\mathrm{surf}}}{N_{\mathrm{tot}}}\frac{\rho_{\mathrm{surf}}}{\rho_{\mathrm{tot}}}\rho_{\mathrm{surf}} = \eta\rho_{\mathrm{surf}}. \quad (2)$$

Note that the k-AO-LDOS unit is states/(eV bohr^{-3}), and that ρ_{surf} is multiplied by the surface component density coefficient η. Similarly, the partial weighted $\rho'(k,E)$ of the arbitrary layer within a surface slab can be analyzed. Here, we concentrate on the surface states of the topmost layer only.

In Fig. 4(d), $\rho'(k,E)$ maps are shown along the $\overline{X}'$-$\overline{\Gamma}$-$\overline{X}$ and $\overline{\Gamma}$-$\overline{M}$ directions. Low density with a 30% threshold was cut for clarity (set as blue background). Surface states with high density are pronounced on the maps. In the valence band, resonance surface state dispersion is expected from −0.5 to −1.0 eV, −2.3 to −2.8 eV, and −3.5 to −4.0 eV. In addition, surface states with high electron density are presented close to −4.8 eV at the $\overline{M}$ point, whereas such surface states are absent at the $\overline{X}$ and $\overline{X}'$ points. The predicted surface states in the valence band could be verified by photoelectron spectroscopy. In this case, the photoelectron intensity is correlated with the electron density of the states in Fig. 4(d).

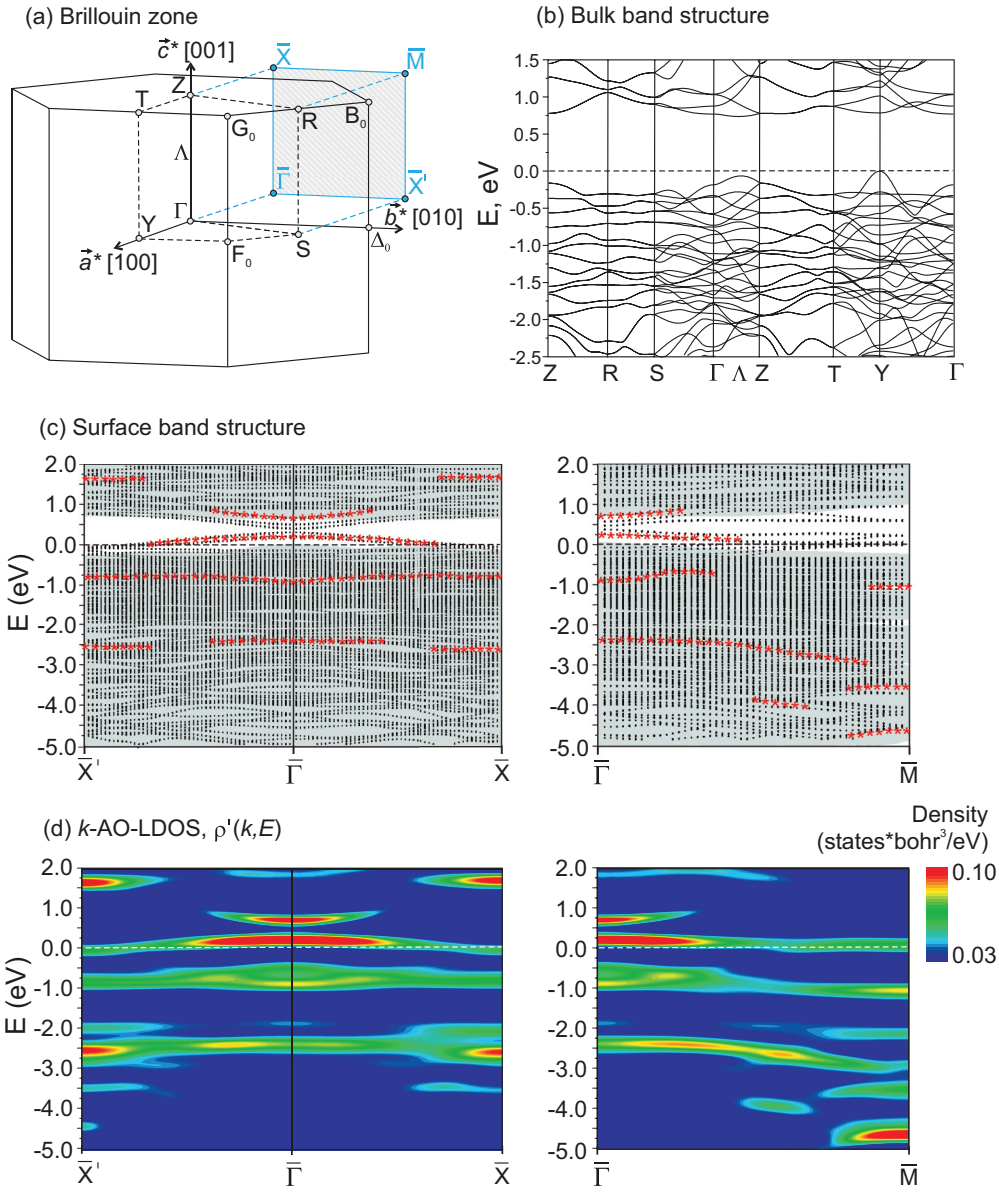

FIG. 4. (Color online) Electronic band structures of β-$FeSi_2$. (a) Schematic Brillouin zone of the bulk β-$FeSi_2$. Surface Brillouin zone of the β-$FeSi_2$-(1×1) reconstruction is shown by blue rectangle. (b) Computed bulk band structure. There is indirect band gap between Y-0.6Λ points. (c) Surface band structure. Grey shaded areas represent projected bulk bands. Black dots correspond to the electronic states of the L_1 model. Surface states induced by the topmost Si layer are marked by red stars. Surface states were identified from the k-projected atomic-orbital based local density of states in (d). Intensity contrast was modulated according to Eq. (2).

A few surface states induced by the topmost atomic layer are also presented in the band gap region and in the conduction band. There are unoccupied states at +0.3 eV and +0.8 eV ($\overline{\Gamma}$ point) and at +1.7 eV ($\overline{X}$ and $\overline{X}'$ points). Surface states in the conduction band can be verified using inverse photoemission measurements [45]. Predicted (resonance) surface states induced by the reconstructed topmost Si layer are summarized in Fig. 4(c) with red stars. The surface states in the band gap (+0.3 eV at $\overline{\Gamma}$ point) cross the Fermi level. These states are responsible for the metallic nature of the film. Previous angle-integrated photoemission measurements indicated metallic behavior of the β-$FeSi_2$/Si(100) thin film [10]. This agrees with our results.

Finally, it is confirmed that the bare epitaxial β-$FeSi_2$ film is metallic. Surface states within a band gap region were identified and related to the topmost Si layer. To obtain the semiconducting electronic properties of the film, these states have to be removed with adsorbate induced reconstruction, for instance. Therefore, identification of the surface states of a bare iron silicide film provide a necessary platform for band gap engineering of the epitaxial β-$FeSi_2$ film and its application in device technology.

V. CONCLUSIONS

An almost single phase of epitaxial β-$FeSi_2$(100)/Si(001)-$p(2 \times 2)$ film was prepared with the SPE method. The surface

atomic structure of epitaxial film was studied by multiple approach methods including quantitative LEED I-V, *ab initio* DFT, and STM. A $p(2 \times 2)$ surface reconstruction with $p2gg$ symmetry was confirmed by LEED. The atomic surface structure was determined by LEED I-V curve analysis: The smallest Pendry's reliability factor $R_P = 0.22 \pm 0.02$ was achieved for the bare Si truncated structure model (L_1). Simulated STM patterns from the best-fit structure model consist of bright protrusions. Each protrusion corresponds to four Si atoms on a surface. The simulated STM patterns agree well with the experimental STM images. The best-fit structure obtained by LEED I-V method agrees well with the structure derived by *ab initio* DFT calculations. Electronic band structures of the bulk and epitaxial β-$FeSi_2$(100) were computed. In contrary to the semiconducting bulk phase, the epitaxial thin β-$FeSi_2$(100) film is metallic. A k-resolved atomic-orbital based local density-of-states analysis was carried out for identification of the surface states. Surface states k-AO-LDOS were decoupled from the bulk-related k-AO-LDOS on the epitaxial β-$FeSi_2$(100) band structure.

ACKNOWLEDGMENTS

Support from the Murata Science Foundation and the Japan Society for the Promotion of Science is highly appreciated. We also would like to thank the Academy of Sciences of the Czech Republic (Project No. M100101201) for their financial support. We thank Y. Morikawa, S. Yanagisawa, I. Hamada, and S. Ohno for fruitful discussion of the paper. The STM simulation was done using the facilities of the Supercomputer Center, the Institute for Solid State Physics, the University of Tokyo.

[1] D. Leong, M. Harry, K. Reeson, and K. Homewood, Nature (London) **387**, 686 (1997).
[2] D. Chi, Thin Solid Films **537**, 1 (2013).
[3] *Binary Alloy Phase Diagrams*, edited by T. Massalski, H. Okamoto, P. Subramanian, and L. Kacprzak (ASM International, Ohio, 1990).
[4] C. Kloc, E. Arushanov, M. Wendl, H. Hohl, U. Malang, and E. Bucher, J. Alloys Compd. **219**, 93 (1995).
[5] E. Arushanov, M. Respaud, J. M. Broto, C. Kloc, J. Leotin, and E. Bucher, Phys. Rev. B **53**, 5108 (1996).
[6] S. Yeo, S. Nakatsuji, A. D. Bianchi, P. Schlottmann, Z. Fisk, L. Balicas, P. A. Stampe, and R. J. Kennedy, Phys. Rev. Lett. **91**, 046401 (2003).
[7] K. Hattori, K. Kataoka, A. Hattori, and H. Daimon, J. Surf. Sci. Soc. Jpn. **29**, 120 (2008).
[8] A. V. de Parga, J. de la Figuera, C. Ocal, and R. Miranda, Europhys. Lett. **18**, 595 (1992).
[9] W. Weiss, M. Kutschera, U. Starke, M. Mozaffari, K. Reshöft, U. Köhler, and K. Heinz, Surf. Sci. **377–379**, 861 (1997).
[10] J. Chrost, J. Hinarejos, P. Segovia, E. Michel, and R. Miranda, Surf. Sci. **371**, 297 (1997).
[11] H. Nakano, K. Maetani, K. Hattori, and H. Daimon, Surf. Sci. **601**, 5088 (2007).
[12] M. Someta, K. Maetani, K. Hattori, and H. Daimon, Surf. Sci. **604**, 21 (2010).
[13] K. Kataoka, K. Hattori, Y. Miyatake, and H. Daimon, Phys. Rev. B **74**, 155406 (2006).
[14] U. Starke, W. Weiss, M. Kutschera, R. Bandorf, and K. Heinz, J. Appl. Phys. **91**, 6154 (2002).
[15] N. Motta, A. Sgarlata, G. Gaggiotti, F. Patella, A. Balzarotti, and M. de Crescenzi, Surf. Sci. **284**, 257 (1993).
[16] J. Gallego, J. Alvarez, J. Hinarejos, E. Michel, and R. Miranda, Surf. Sci. **251–252**, 59 (1991).
[17] I. Goldfarb, Surf. Sci. **554**, L87 (2004).
[18] Y. Dusausoy, J. Protas, R. Wandji, and B. Roques, Acta Crystallogr. B **27**, 1209 (1971).
[19] S. J. Clark, H. M. Al-Allak, S. Brand, and R. A. Abram, Phys. Rev. B **58**, 10389 (1998).
[20] D. Peale, R. Haight, and J. Ott, Appl. Phys. Lett. **62**, 1402 (1993).
[21] J. E. Mahan, V. L. Thanh, J. Chevrier, I. Berbezier, J. Derrien, and R. G. Long, J. Appl. Phys. **74**, 1747 (1993).
[22] H.-U. Nissen, E. Müller, H. Deller, and H. von Kanel, Phys. Status Solidi A **150**, 395 (1995).
[23] M. Tanaka, Y. Kumagai, T. Suemasu, and F. Hasegawa, Jpn. J. Appl. Phys. **36**, 3620 (1997).
[24] F. Shoji, H. Shimoji, Y. Makihara, and M. Naitoh, Thin Solid Films **461**, 116 (2004).
[25] W. Raunau, H. Niehus, and G. Comsa, Surf. Sci. Lett. **284**, L375 (1993).
[26] S. Hajjar, G. Garreau, S. Pelletier, P. Bertoncini, P. Wetzel, G. Gewinner, M. Imhoff, and C. Pirri, Surf. Sci. **532–535**, 940 (2003).
[27] Y. Yamada, I. Wakaya, S. Ohuchi, H. Yamamoto, H. Asaoka, S. Shamoto, and H. Udono, Surf. Sci. **602**, 3006 (2008).
[28] S. Tanimoto and T. Nagano, Phys. Procedia **11**, 146 (2011).
[29] A. Barbieri and M. A. V. Hove, Symmetrized Automated Tensor LEED package (SATLEED), available from M. A. Van Hove.
[30] A. Barbieri and M. A. V. Hove, SPHASE shift calculation package, available from M. A. Van Hove.
[31] J. B. Pendry, J. Phys. C: Solid State Phys. **13**, 937 (1980).
[32] *International Tables for Crystallography*, Vol. A, 5th ed., edited by T. Hahn (Kluwer Academic, Dordrecht, 2002).
[33] V. Blum and K. Heinz, Comput. Phys. Commun. **134**, 392 (2001).
[34] S. Higashi, T. Shirasawa, S. Mizuno, and H. Tochihara, Surf. Sci. **588**, 167 (2005).
[35] V. B. Nascimento, R. G. Moore, J. Rundgren, J. Zhang, L. Cai, R. Jin, D. G. Mandrus, and E. W. Plummer, Phys. Rev. B **75**, 035408 (2007).
[36] Y. Morikawa, Phys. Rev. B **63**, 033405 (2001).
[37] J. P. Perdew, K. Burke, and M. Ernzerhof, Phys. Rev. Lett. **77**, 3865 (1996).
[38] K. Hermann and M. A. V. Hove, LEEDPAT simulation program, version 2.1, 2006.
[39] Y. Yamada, W. Mao, H. Asaoka, H. Yamamoto, F. Esaka, H. Udonob, and T. Tsurud, Phys. Procedia **11**, 67 (2011).

[40] *Modern Diffraction Methods*, 1st ed., edited by E. Mittemeijer and U. Welzer (Wiley-VCH Verlag, Weinheim, 2013).

[41] M. Wießner, J. Ziroff, F. Forster, M. Arita, K. Shimada, P. Puschnig, A. Schöll, and F. Reinert, Nat. Commun. **4**, 1514 (2013).

[42] *Principles of Surface Physics*, edited by F. Bechstedt (Springer-Verlag, Berlin, 2003).

[43] E. G. Moroni, W. Wolf, J. Hafner and R. Podloucky, Phys. Rev. B **59**, 12860 (1999).

[44] K. Toyoda, I. Hamada, S. Yanagisawa and Y. Morikawa, Appl. Phys. Express **3**, 025701 (2010).

[45] *Surface Science - An Introduction*, edited by K. Oura, V. G. Lifshits, A. A. Saranin, A. V. Zotov, M. Katayama (Springer-Verlag, Berlin, 2003).